Journal of Materials Chemistry A

ROYAL SOCIETY OF CHEMISTRY

PAPER

View Article Online
View Journal | View Issue

Cite this: J. Mater. Chem. A, 2022, 10, 25063

A photofunctional platform of bis-terpyridine ruthenium complex-linked coordination polymers with structural diversity†‡

Aichun Wu, Yuanlin Tang, Xinling Li, Baohua Zhang, Aiju Zhou, Zhiwei Qiao * and Lianpeng Tong *

Received 14th September 2022
Accepted 3rd November 2022

DOI: 10.1039/d2ta07219j

rsc.li/materials-a

Solvothermal syntheses of the bis(4′-carboxyl-2,2′:6′,2″-terpyridine) ruthenium complex [Ru(tpyCOO$^-$)$_2$] as a linker and different metal anions as nodes constructed a family of ten novel coordination polymers (CPs) with different topological types, ranging from one-dimensional (1D) chains and two-dimensional (2D) networks to three-dimensional (3D) frameworks. The structural diversity of CPs is achieved by the various coordinating geometries of metal nodes, including 3d transition (monometallic or bimetallic), lanthanide, and group 4 (zirconium and hafnium) metal anions. The Ru complex linker plays the role of a light-harvesting unit and renders multifarious photofunctions to the CP materials. While the ytterbium CP (**Yb–Ru**) exhibits near-infrared emission upon visible-light excitation, the 2D bimetallic Co/Ni CPs (**Co$_x$–Ni$_y$–Ru**) and 3D interpenetrated copper CP (**Cu–Ru**) show high to modest efficiencies toward the photocatalytic hydrogen evolution reaction. We suggest the series of new CPs with versatile structural traits as a unique platform for the research of photocatalysis and other photonic functional applications.

Introduction

Coordination polymers (CPs), also known as metal–organic frameworks (MOFs), have emerged as a class of porous crystalline materials that attracted great interest across interdisciplinary research fields during the past decades.[1–6] One unique merit of CP materials is that their topological structures can be elaborately designed and modified at the molecular level by the choice of the building components—organic linkers and inorganic nodes. The chemical and physical properties of CPs at the macroscopic level, otherwise, are determined by their geometrical morphology as well as the intrinsic features of their inorganic and organic building units. Incorporation of photo- and redox-active units in the construction of CPs may not only enhance the original functionalities of these building components but also generate new functionalities, due to the potential synergistic effect between the components within the specifical spatial environments of CPs.[7–15] Recent studies have shown promising applications of photosensitizer-incorporated CPs in the areas of photosynthesis,[16–21] photocatalysis,[9,22–27] light-emitting materials,[28–30] sensor materials,[28,31–34] and light-harvesting complexes.[35–37]

Polypyridyl ruthenium complexes are classic molecular photosensitizers with long-lived excited states and unique redox properties.[38] The porous architectures of CPs built from polypyridyl Ru(II) photosensitizers have shown outstanding performance in photocatalysis, especially reactions related to solar fuel production.[39–46] However, the tedious preparation of polypyridyl Ru(II) complexes and problematic crystallization of the frameworks, which might be attributed to the positive charge of the Ru(II) center and the obstacle of bulky polypyridyl ligands, have raised severe limitations over the research and development of functional CPs based on Ru(II) complex linkers.[45,47–49] Systematic synthesis of polypyridyl Ru(II) complex-linked CPs with various metal nodes and versatile topological structures is rarely reported.

We recently reported the syntheses of a series of two-dimensional (2D) CPs comprising bis(4′-carboxyl-2,2′:6′,2″-terpyridine) ruthenium linker [Ru(tpyCOO$^-$)$_2$], which was readily prepared from commercially available compounds, and 3d transition-metal (Mn, Co, Ni, and Zn) nodes (Scheme 1a).[50] These 2D coordination networks are capable of driving highly efficient photocatalytic hydrogen evolution from water without the assistance of any co-catalysts or co-sensitizers. The current work describes our effort of systematically assembling the [Ru(tpyCOO$^-$)$_2$] linker with various metal nodes and further outspreading a family of novel CPs. Besides the previous 2D monometallic coordination networks,[50] we report here four categories of coordination polymers based on the same

School of Chemistry and Chemical Engineering, Guangzhou University, Higher Education Mega Center, No. 230 Wai Huan Xi Road, Guangzhou, 510006, P. R. China. E-mail: zqiao@gzhu.edu.cn; ltong@gzhu.edu.ch

† This paper is dedicated to Prof. Licheng Sun on the occasion of his 60th birthday.

‡ Electronic supplementary information (ESI) available. CCDC 2009804, 2024242, 2024244, 2024245, 2178964 and 2178965. For ESI and crystallographic data in CIF or other electronic format see DOI: https://doi.org/10.1039/d2ta07219j

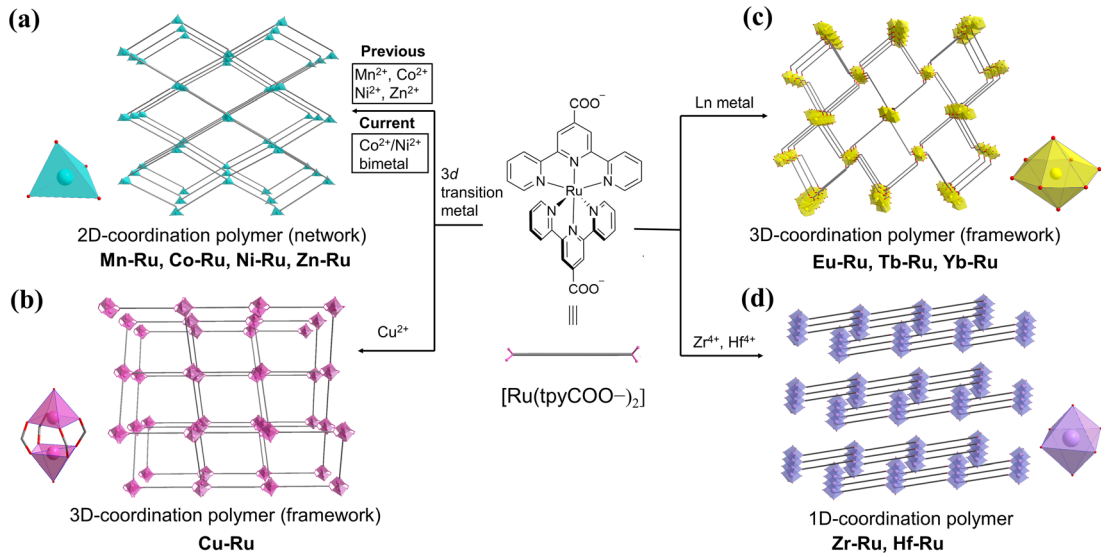

Scheme 1 Overview of the four classes of coordination polymers built from the $[Ru(tpyCOO^{-})_2]$ linker and various metal anion nodes, with schematic topologies in their single crystal structures. (a) 2D bimetallic Co/Ni CPs, (b) 3D Cu CP, (c) 3D lanthanide CPs, and (d) 1D Zr and Hf CPs.

$[Ru(tpyCOO^{-})_2]$ linker: mixed Co^{2+}/Ni^{2+} cations and $[Ru(tpyCOO^{-})_2]$ affording bimetallic 2D coordination networks **Co$_x$–Ni$_y$–Ru** (Scheme 1a), Cu^{2+} nodes bridged by $[Ru(tpyCOO^{-})_2]$ affording an interpenetrated 3D coordination framework **Cu–Ru** (Scheme 1b), Ln nodes affording isostructural 3D coordination frameworks **Ln–Ru** (**Ln** = **Eu**, **Tb**, or **Yb**, Scheme 1c), and group 4 Zr^{4+} and Hf^{4+} nodes affording 1D coordination chains **Zr–Ru** and **Hf–Ru** (Scheme 1d). The structural diversity of these $[Ru(tpyCOO^{-})_2]$-linked CPs explicitly demonstrates the viability of designing and tuning the crystalline structures of coordination polymers at the molecular level.

More importantly, integrating the light-harvesting $[Ru(tpyCOO^{-})_2]$ component with different metal nodes provides a unique CP platform of multifarious photofunctions.[10,51–53] While the photoluminescence spectrum of **Yb–Ru** shows emission at 976 nm upon excitation of the $[Ru(tpyCOO^{-})_2]$ linker unit, the bimetallic Co^{2+}/Ni^{2+} coordination networks (**Co$_x$–Ni$_y$–Ru**) are efficient catalysts for the visible-light driven hydrogen evolution reaction. More interesting photofunctions are expected to be studied and exploited based on this CP platform *via* further constituent optimization or post-synthetic modification of the coordination frameworks.[54,55]

Results and discussion

Syntheses and structures

(i) 2D bimetallic Co/Ni coordination polymers. In the previous work, we have reported the solvothermal reaction of $[Ru(tpyCOOH)_2]^{2+}$ with $Co(NO_3)_2$ or $Ni(ClO_4)_2$ affording crystalline $\{0.5Co\cdot[Ru(tpyCOO^{-})_2]\cdot PF_6\}$ and $\{0.5Ni\cdot[Ru(tpyCOO^{-})_2]\cdot PF_6\}$ coordination polymers denoted as **Co–Ru** and **Ni–Ru**, respectively.[50] These two isomeric CPs possess a 2D coordination network topology (**sql**, 4^4) and are readily exfoliated into ultrathin coordination polymer nanosheets that comprise several lattice layers.

By following the previous synthetic conditions for **Co–Ru** and **Ni–Ru**, we prepared 2D bimetallic Co/Ni coordination polymers as micro crystals denoted as **Co$_x$–Ni$_y$–Ru**, where the subscripts x and y represent the molar ratio of $Co(NO_3)_2$ and $Ni(ClO_4)_2$ salt precursors used in the syntheses (x/y = 1/1, 1/2, 1/4, and 1/6). The field-emission scanning electron microscopy (FE-SEM) images of **Co$_x$–Ni$_y$–Ru** (Fig. S12,‡ taking **Co$_1$–Ni$_2$–Ru** as an example) display layered structures similar to the structural features of **Co–Ru** and **Ni–Ru** reported previously. The powder X-ray diffraction (PXRD) patterns of the bimetallic **Co$_x$–Ni$_y$–Ru** bulk samples (Fig. S7‡) with different x/y ratios show identical peaks to the PXRD patterns of **Co–Ru** or **Ni–Ru**, indicating the same 2D morphology of **Co$_x$–Ni$_y$–Ru** as that of **Co–Ru** or **Ni–Ru**.[50] Inductively coupled plasma mass spectrometry (ICP-MS) confirms the contents of both Co and Ni ions in the Co$_x$–Ni$_y$–Ru products (Table S8‡). The measured molar metal ratios (n_{Co}/n_{Ni}) in the bimetallic CPs range from n_{Co}/n_{Ni} = 15.2 (x/y = 1/1) to n_{Co}/n_{Ni} = 1.7 (x/y = 1/6).

Ultrasonication in protic solvents allows exfoliation of the bimetallic Co/Ni CPs into thin nanosheets, which are shown by both the FE-SEM and transmission electron microscopy (TEM) images (Fig. 1 and S13–S15‡) of the ultrasonicated suspension.

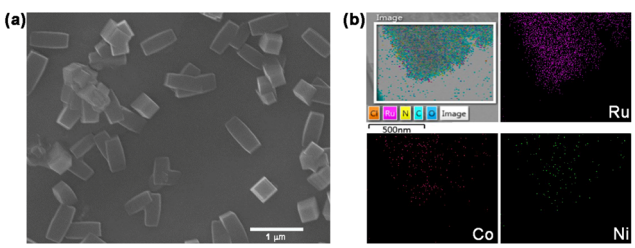

Fig. 1 (a) FE-SEM images of exfoliated **Co$_1$–Ni$_2$–Ru** nanosheets. (b) TEM image and elemental mapping of exfoliated **Co$_1$–Ni$_2$–Ru** nanosheets.

At the same time, the element mapping identified the presence of both Ni and Co metal elements in the **Co$_x$–Ni$_y$–Ru** nanosheets (Fig. 1 and S15‡). The PXRD patterns of bimetallic CP nanosheets maintain all characteristic diffraction peaks of their networks prior to the exfoliation (Fig. S8,‡ taking **Co$_1$–Ni$_4$–Ru** as an example), indicating the preserved 2D coordination lattices in the nanosheets. These nanosheets are estimated to consist of 3–7 layers of 2D lattices with a thickness of 2–6 nm.[50] The X-ray photoelectron spectroscopy (XPS) spectra of **Co$_1$–Ni$_4$–Ru** (Fig. S16 & S17‡) show binding energy peaks at 781.53 eV and 797.65 eV together with satellite peaks at 786.0 eV and 802.41 eV that are ascribed to the Co(II) ion.[56,57] Further the XPS Ni 2p scan of **Co$_1$–Ni$_4$–Ru** (Fig. S18‡) illustrates peaks at 855.98 eV and 873.34 eV, suggesting the presence of the Ni(II) ion.[58]

(ii) 3D Cu coordination polymer. The copper coordination polymer, **Cu–Ru**, was solvothermally prepared in DMF using $CuCl_2$ and $[Ru(tpyCOOH)_2]^{2+}$. Single-crystal structure analysis of **Cu–Ru** revealed the two-fold interpenetration **cds** ($6^5\cdot8$) topology of this coordination framework, which is composed of paddlewheel cupric nodes (Fig. 2 and S1‡) and the Ru complex linker. Each dimeric copper node, with a Cu···Cu separation of 2.6389(11) Å, is coordinated by four μ_2-bridging carboxylate groups of distinct $[Ru(tpyCOO^-)_2]$ linkers in a square bipyramid manner. The two axial sites of the Cu–Cu vector are both occupied by the DMF oxygen atoms. The equatorial Cu–O (carboxylate) bond lengths range from 1.947(4) to 1.986(4) Å while the axial Cu–O (DMF) distances are between 2.114(5) and 2.114(5) Å (Table S2‡). The elongation of these axial Cu–O bonds has been widely observed in the paddlewheel cupric centers due to the Jahn–Teller effect. The O–Cu–O angles in the Cu-carboxylate coordination plane fall in the range of 88.37(17)° to 90.68(17)° (Table S5‡). The framework is electrically positively charged; both chloride (from the $CuCl_2$ precursor) and PF_6^- (from the Ru complex) counterions can be identified by X-ray diffraction in the porous vacancy. The composition of **Cu–Ru** can be formulated as $\{Cu\cdot[Ru(tpyCOO^-)_2]\cdot DMF\cdot0.5Cl\cdot1.5PF_6\}$.

(iii) 3D lanthanide coordination polymers. Lanthanide CPs, including **Eu–Ru**, **Tb–Ru** and **Yb–Ru**, were prepared *via* solvothermal methods using lanthanide nitrates and $[Ru(tpyCOOH)_2]^{2+}$ as the reactants. The obtained crystalline precipitates of these three lanthanide CPs were resolved by single-crystal X-ray diffraction to be isostructural frameworks and therefore, only the structure of **Tb–Ru** was described here as an example (Fig. 3 and S3‡). There are two crystallographically

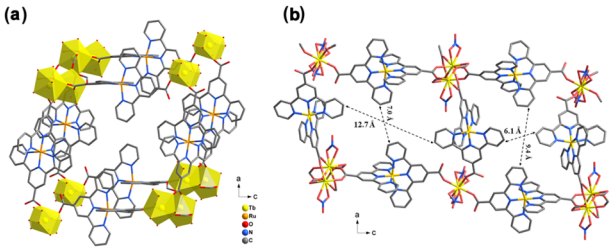

Fig. 3 (a) Stick-polyhedron representation of the **Tb–Ru** single crystal structure (used as an example for lanthanide CPs) viewed along the *b* axis direction, where the yellow polyhedron represents terbium nodes. (b) The **sql** ($4^4\cdot6^2$) coordination topology of **Tb–Ru**.

independent mononuclear Tb(III) nodes in the crystal structure. The Tb1 ion adopts a coordination geometry of capped square antiprism with nine oxygen atoms, of which four are donated by the carboxylates of Ru linkers, two by a μ_2-nitrate, two by a μ_2-formate and one by a μ_1-formate (Fig. S4‡). The Tb2 ion is coordinated by eight oxygen atoms from four μ_1-carboxylates of the Ru linkers and two μ_2-nitrates, of which one isotropic NO_3^- plane is parallel or perpendicular to the other (Fig. S5‡). The Tb1 and Tb2 ions, both acting as 4-connected nodes, form two inorganic chains as the skeleton of a 3D framework. Accordingly, the framework of **Tb–Ru**, as well as **Eu–Ru** and **Yb–Ru**, possesses two types of one-dimensional channels with different diameters and can be abstracted into a **sql** ($4^4\cdot6^2$) topology (Fig. 3 and S3‡). Non-binding nitrate or PF_6^- counterions are trapped in the channels to balance the charge of lanthanide ions. The formula of **Tb–Ru** can be written as $\{1.5Tb\cdot2[Ru(tpyCOO^-)_2]\cdot3NO_3\cdot0.5PF_6\cdot HCOO^-\}$. The compositions of counterions for **Eu–Ru** and **Yb–Ru** are slightly different (see the synthesis section in ESI‡).

(iv) 1D Zr or Hf coordination polymer. The zirconium and hafnium CPs, **Zr–Ru** and **Hf–Ru**, were prepared as dark red crystals under solvothermal conditions. The single-crystal X-ray diffraction analysis reveals isostructural coordination chains of these two CPs and thus only the structure of **Zr–Ru** is discussed here as an example. As shown in Fig. 4, each Zr(IV) is coordinated with six oxygen atoms from two μ_1-carboxylates of discrete $[Ru(tpyCOO^-)_2]$ linkers and four hydroxy groups of solvent water molecules, forming a ZrO_6 octahedra node (Fig. S6‡). These linked Zr nodes and Ru complexes produce infinite one-dimensional chains parallel to each other along the *a*-axis. The individual chains align *via* the edge-to-face π–π interaction and

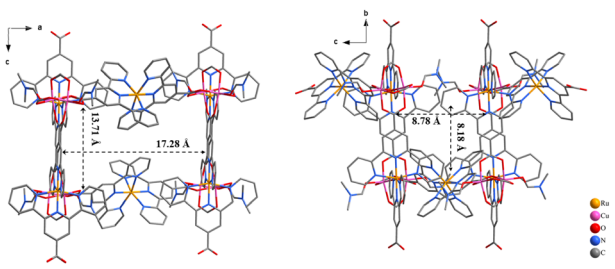

Fig. 2 Stick representation of the **Cu–Ru** single crystal structure, showing the **cds** ($6^5\cdot8$) coordination topology.

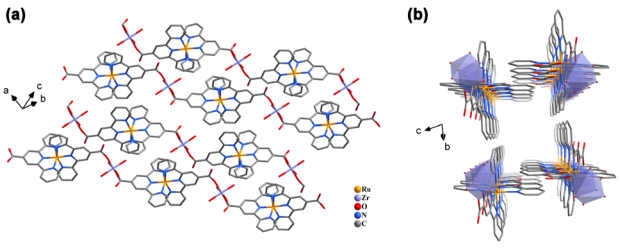

Fig. 4 (a) Stick-polyhedron representation of the **Zr–Ru** single crystal structure. (b) Selected adjacent coordination chains showing the interactions and void space in the structure.

DMF molecules are observed in the void space between the coordination chains. Elemental analysis (C, N, H) of **Zr–Ru** and **Hf–Ru** suggests the presence of disordered PF_6^- and Cl^- counterions trapped in the lattice of these coordination polymers.

Characterization and properties

The thermogravimetric analysis (TGA) demonstrates that all four categories of CPs begin to lose non-coordinating DMF and water molecules below 100 °C (Fig. S19–S22‡). A significant weight loss of these CPs occurs at higher temperatures ranging from 260 °C (for the bimetallic Co/Ni CPs) to 400 °C (for the Zr and Hf CPs), due to the degradation of the coordination frameworks. The N_2 sorption measurement of **Cu–Ru** at 77 K reveals a type II isotherm (Fig. S23‡), corresponding to a Brunauer–Emmett–Teller (BET) surface area of 1.9 $m^2\ g^{-1}$. The N_2 sorption isotherm of **Yb–Ru** (Fig. S24‡), as an example of the Ln CPs, indicates a BET surface area of 7.6 $m^2\ g^{-1}$. The weak N_2 gas adsorption capability of these 3D CPs is ascribed to the presence of counterions that occupy the porous space within the crystal frameworks. In addition, the interpenetrated structure of **Cu–Ru** makes it almost imporous.

The cyclic voltammogram (CV) of the bimetallic Co/Ni CP, taking **Co_1–Ni_2–Ru** as an example, displays redox waves at −1.6 and −2.0 V *versus* ferrocenium/ferrocene (Fc^+/Fc, Fig. S26‡). Very similar redox features have been reported for the previously synthesized **Co–Ru** or **Ni–Ru** CPs and assigned to the redox events of [Ru(tpyCOO$^-$)$_2$] linkers.[50] Such characteristic redox features at −1.6 and −2.0 V were also observed in the CVs of **Cu–Ru** and the lanthanide CPs (Fig. S27 and S28‡). Despite the different metal nodes and various structures of these CPs, they all retain the redox properties of the bis-terpyridine ruthenium complex.

The solid-state UV-vis absorption spectra of these CPs all exhibit broad absorbance bands at about 300 nm and 500 nm, besides shoulder absorbance bands of some CP samples at 550 nm (Fig. S30–S33‡). These longer-wave bands in the visible light region are attributed to the characteristic metal-to-ligand charge transfer (MLCT) of [Ru(tpyCOO$^-$)$_2$] linkers, while the short-wave bands at 300 nm originate from the π–π* excitation of tpy ligands. The solid-state emission bands of 3d transition-metal-based CPs, **Co_x–Ni_y–Ru** and **Cu–Ru**, are centered at approximately 670–690 nm (Fig. S36‡),[50] while the emission bands of lanthanide CPs are centered at about 670 nm (Fig. S37‡). The emission spectrum of [Ru(tpyCOOH)$_2$](PF$_6$)$_2$ powder exhibits a broad band at λ_{max} = 720 nm. These absorption and emission studies emphasize that the CPs preserve the photophysical properties of the Ru complex linker, whereas various coordinating metal nodes slightly alter the ground/excited states of the Ru linker unit.

Since the Yb(III) ion emits luminescence in the near-infrared (NIR) range distinctively separated from the emission of the Ru linker in the visible-light range, the photochemical properties of **Yb–Ru** were further investigated. Upon excitation of the Ru linker of **Yb–Ru** at λ_{ex} = 580 nm, a sharp NIR emission band at 978 nm assigned to the $^2F_{5/2} \rightarrow {}^2F_{7/2}$ transition of the Yb(III) ion[59] was observed in the spectrum (Fig. 5), besides the characteristic Ru linker luminescent band at 670 nm (Fig. S37‡). Meanwhile, the excitation spectrum of **Yb–Ru** recorded upon the NIR luminescent band (λ_{em} = 976 nm) shows very similar featured bands to the excitation spectrum of the [Ru(tpyCOOH)$_2$](PF$_6$)$_2$ complex (λ_{em} = 720 nm, Fig. 5). The excitation spectra of **Yb–Ru** collected upon the Yb(III) node emission (λ_{em} = 976 nm) and the Ru linker emission (λ_{em} = 670 nm) adopt similar profiles (Fig. S37‡). These spectroscopic results suggest that the Yb(III) node of **Yb–Ru** can be excited by the MLCT stated of the Ru linker, which plays the role of a sensitizer, tentatively *via* an energy transfer process.[60–62] The time-resolved photoluminescence experiments (Fig. S38‡) reveal a reduced decay time of the excited [Ru(tpyCOOH)$_2$]$^{2+}$ complex upon coordination to the Yb(III) ions in **Yb–Ru**, consistent with the proposed energy transfer process throughout the CP framework.[49,63]

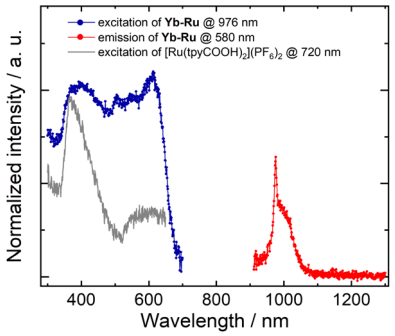

Fig. 5 Near-IR emission (red dot, λ_{ex} = 580 nm) and excitation (blue dot, λ_{em} = 976 nm) profiles of **Yb–Ru** solid powder, and the excitation profile (grey line, λ_{em} = 720 nm) of the [Ru(tpyCOOH)$_2$](PF$_6$)$_2$ complex in the solid state.

Photocatalytic hydrogen evolution

In the previous study, 2D **Co–Ru** and **Ni–Ru** nanosheets have been shown to effectively drive photocatalytic hydrogen evolution from an aqueous solution under the irradiation of visible light (λ > 420 nm).[50] No co-catalyst or co-sensitizer was required for this photocatalytic hydrogen evolution process. The hydrogen evolution reaction is proposed to be initiated by quenching of the excited [Ru(tpyCOO$^-$)$_2$] linker. The resulting formally monovalent Ru(I) species transfer electrons to the Co or Ni nodes at the edge of CP nanosheets, where the reduction of protons occurs. The driving force for photocatalytic hydrogen evolution originates from the energy gap between the LUMO level of the [Ru(tpyCOO$^-$)$_2$] linker and the hydrogen evolution potential. Because the bimetallic Co/Ni CPs, the **Cu–Ru**, and the lanthanide CPs maintain the photochemical and electrochemical properties of the [Ru(tpyCOOH)$_2$](PF$_6$)$_2$ complex, they were assessed for photocatalytic hydrogen evolution after being dispersed in aqueous solution. Sonicating **Zr–Ru** and **Hf–Ru** in aqueous solution leads to decomposition of these two CPs and thus their photocatalytic activity towards hydrogen evolution was not investigated.

Under the irradiation of visible light (λ > 420 nm), the exfoliated **Co_x–Ni_y–Ru** CP nanosheets effectively produced hydrogen from ascorbic acid solution without the presence of any co-catalysts or co-sensitizers (Fig. 6, S39 and S40‡). A pH range

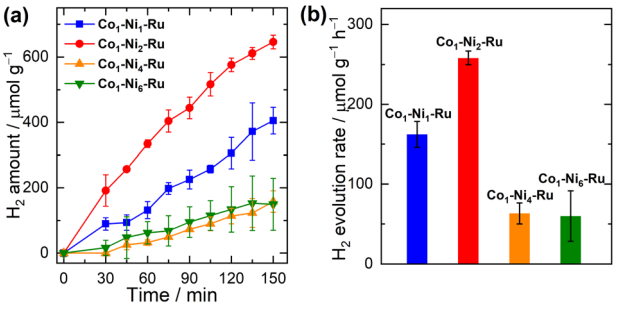

Fig. 6 (a) Photocatalytic hydrogen evolution by 2D bimetallic Co/Ni CPs under visible-light irradiation (λ > 420 nm) from ascorbic acid solution (0.5 M, pH = 4.0). (b) Initial photocatalytic hydrogen evolution rates (μmol g^{-1} h^{-1}) for different 2D bimetallic Co/Ni CPs.

from 3 to 5 was tested and pH = 4 was found optimal for the photocatalytic performance of these CPs (Fig. S41‡). Among the four 2D bimetallic Co/Ni CPs, **Co_1–Ni_2–Ru** achieved the greatest initial reaction rate of 258 ± 8 μmol g^{-1} h^{-1}, producing the most hydrogen amount of 645 ± 8 μmol g^{-1} in the 2.5 h reaction period (Fig. 6). More Ni content in the cases of **Co_1–Ni_4–Ru** and **Co_1–Ni_6–Ru** than **Co_1–Ni_2–Ru** significantly suppressed the photocatalytic hydrogen evolution activity, and the initial hydrogen evolution rates for **Co_1–Ni_4–Ru** and **Co_1–Ni_6–Ru** are merely 63 ± 13 and 60 ± 31 μmol g^{-1} h^{-1}.

Based on our previous investigation,[50] we propose that the photocatalytic hydrogen evolution by **Co_x–Ni_y–Ru** nanosheets undergoes a reductive quenching pathway, where the excited Ru linker is first reduced by the sacrificial donor and then transfers one electron to the Co/Ni node. The driving force for the photocatalytic reaction is estimated to be about 0.7 eV at pH = 4.0, according to the redox potentials of Co/Ni CPs (Fig. S43‡). The critical step of the catalytic cycle is believed as proton association with the reduced and unsaturated Ni or Co node. Even though the previous findings concluded the more catalytically efficient Ni node at the edge of nanosheets than the edge Co node, a too large portion of Ni ions present in the bimetallic Co/Ni CPs might create a significant number of defective sites and thus hinder the electron transfer within the bimetallic CP nanosheets. In addition, these defective sites are detrimental to the completeness of CP crystalline and reduce the amount of active catalytic nodes at the edge of nanosheets.

The **Cu–Ru** coordination polymer, after being dispersed by ultrasonic treatment, is also able to catalyze visible-light driven hydrogen evolution in the pH = 4 ascorbic acid solution with a modest reaction rate of 151 ± 19 μmol g^{-1} h^{-1} (Fig. S42‡). In contrast, the lanthanide CP **Eu–Ru**, **Tb–Ru** or **Yb–Ru** does not display photocatalytic activity under the same light-driven hydrogen evolution conditions described above. The type of metal nodes rather than the topologies of CPs is ascribed to the photocatalytic disparity.

Conclusions

In the present work, we synthesized a family of ten coordination polymers composed of Ru(II) linker [Ru(tpyCOO$^-$)$_2$] and different metal cations, including the mixed bimetallic Co/Ni ion nodes. Single-crystal X-ray diffraction analysis revealed topological diversity of these porous coordination polymers depending on the type of metal ions. The series of CPs provide a promising platform for the development of multifarious functionalities based on the photochemical properties of the polypyridyl Ru linker. The obtained CPs were screened as catalysts for the photocatalytic hydrogen evolution reaction. Both the 2D bimetallic Co/Ni CP (**Co_x–Ni_y–Ru**) and 3D copper CP (**Cu–Ru**) showed notable catalytic performance without the addition of co-catalysts or co-sensitizers. Moreover, the 3D yttrium CP (**Yb–Ru**) exhibited characteristic near-infrared emission upon excitation of the ruthenium complex linker. These results elaborately demonstrate how various structures and functions of CPs derive from the interplay of their organic and inorganic components. Design and syntheses of CPs based on novel bis-terpyridine ruthenium complex derivatives are now in progress, aiming at further development of multifunctional materials.

Author contributions

L. Tong and Z. Qiao conceived the concept and designed the experiments. L. Tong supervised this study. A. Wu, Y. Tang, and X. Li prepared the samples, conducted the characterization, and assessed the catalytic activity. B. Zhang carried out the photochemical investigation and processed the data. A. Zhou resolved the single crystal X-ray diffraction data and determined the CP structures. All authors discussed the results, contributed to the manuscript writing, and approved its final version.

Conflicts of interest

There are no conflicts to declare.

Acknowledgements

This work is supported by Guangzhou University under the funding number of 202201020230, and the State Key Laboratory of Fine Chemicals, Dalian University of Technology (KF2014). We also gratefully thank the National Natural Science Foundation of China (21978058 and 21676094), the Pearl River Talent Recruitment Program (2019QN01L255) and the R & D Program of the Joint Institute of GZHU and ICoST (GI202102) for financial support.

Notes and references

1 S. R. Batten, N. R. Champness, X.-M. Chen, J. Garcia-Martinez, S. Kitagawa, L. Öhrström, M. O'Keeffe, M. P. Suh and J. Reedijk, *CrystEngComm*, 2012, **14**, 3001–3004.
2 S. R. Batten, S. M. Neville and D. R. Turner, *Coordination Polymers: Design, Analysis and Application*, The Royal Society of Chemistry, 2009.
3 J. R. Long and O. M. Yaghi, *Chem. Soc. Rev.*, 2009, **38**, 1213–1214.

4 S. R. Batten, N. R. Champness, X.-M. Chen, J. Garcia-Martinez, S. Kitagawa, L. Öhrström, M. O'Keeffe, M. Paik Suh and J. Reedijk, *Pure Appl. Chem.*, 2013, **85**, 1715–1724.
5 U. Ryu, S. Jee, P. C. Rao, J. Shin, C. Ko, M. Yoon, K. S. Park and K. M. Choi, *Coord. Chem. Rev.*, 2021, **426**, 213544.
6 A. Kirchon, L. Feng, H. F. Drake, E. A. Joseph and H. C. Zhou, *Chem. Soc. Rev.*, 2018, **47**, 8611–8638.
7 H. Furukawa, K. E. Cordova, M. O'Keeffe and O. M. Yaghi, *Science*, 2013, **341**, 1230444.
8 Y. B. Huang, J. Liang, X. S. Wang and R. Cao, *Chem. Soc. Rev.*, 2017, **46**, 126–157.
9 J. D. Xiao and H. L. Jiang, *Acc. Chem. Res.*, 2019, **52**, 356–366.
10 Y. Cui, B. Li, H. He, W. Zhou, B. Chen and G. Qian, *Acc. Chem. Res.*, 2016, **49**, 483–493.
11 S. Fu, S. Yao, S. Guo, G. C. Guo, W. Yuan, T. B. Lu and Z. M. Zhang, *J. Am. Chem. Soc.*, 2021, **143**, 20792–20801.
12 S. N. Sun, L. Z. Dong, J. R. Li, J. W. Shi, J. Liu, Y. R. Wang, Q. Huang and Y. Q. Lan, *Angew. Chem., Int. Ed.*, 2022, **61**, e202207282.
13 S. J. Yao, N. Li, J. Liu, L. Z. Dong, J. J. Liu, Z. F. Xin, D. S. Li, S. L. Li and Y. Q. Lan, *Inorg. Chem.*, 2022, **61**, 2167–2173.
14 J. Zhang, Y. Wang, H. Wang, D. Zhong and T. Lu, *Chin. Chem. Lett.*, 2022, **33**, 2065–2068.
15 T. Lu, T. Li, D. Shi, J. Sun, H. Pang, L. Xu, J. Yang and Y. Tang, *SmartMat*, 2021, **2**, 591–602.
16 Z.-Y. Gu, J. Park, A. Raiff, Z. Wei and H.-C. Zhou, *ChemCatChem*, 2014, **6**, 67–75.
17 Y. Guo, Y. Wang, Y. Shen, Z. Cai, Z. Li, J. Liu, J. Chen, C. Xiao, H. Liu, W. Lin and C. Wang, *J. Am. Chem. Soc.*, 2020, **142**, 21493–21501.
18 S. Li, Y. Gao, N. Li, L. Ge, X. Bu and P. Feng, *Energy Environ. Sci.*, 2021, **14**, 1897–1927.
19 X. Y. Zhang, C. F. Xie, S. Q. Wang, X. M. Cheng, Y. Zhang, Y. Zhao, Y. Lu and W. Y. Sun, *Inorg. Chem.*, 2022, **61**, 1590–1596.
20 N.-Y. Huang, J.-Q. Shen, X.-W. Zhang, P.-Q. Liao, J.-P. Zhang and X.-M. Chen, *J. Am. Chem. Soc.*, 2022, **144**, 8676–8682.
21 J. Zhang, D. Zhong and T. Lu, *Acta Phys.-Chim. Sin.*, 2021, **37**, 2008068.
22 A. Dhakshinamoorthy, A. M. Asiri and H. Garcia, *Angew. Chem., Int. Ed.*, 2016, **55**, 5414–5445.
23 H. Wang, Q.-L. Zhu, R. Zou and Q. Xu, *Chem*, 2017, **2**, 52–80.
24 X. Feng, Y. Pi, Y. Song, C. Brzezinski, Z. Xu, Z. Li and W. Lin, *J. Am. Chem. Soc.*, 2020, **142**, 690–695.
25 H. An, H. Luo, T. Xu, S. Chang, Y. Chen, Q. Zhu, Y. Huang, H. Tan and Y. G. Li, *Inorg. Chem.*, 2022, **61**, 10442–10453.
26 Y. N. Gong, J. W. Liu, J. H. Mei, X. L. Lin, J. H. Deng, X. Li, D. C. Zhong and T. B. Lu, *Inorg. Chem.*, 2021, **60**, 14924–14931.
27 J. H. Zhang, Y. N. Gong, H. J. Wang, Y. C. Wang, W. Yang, J. H. Mei, D. C. Zhong and T. B. Lu, *Proc. Natl. Acad. Sci. U. S. A.*, 2022, **119**, e2118278119.
28 H. Q. Yin and X. B. Yin, *Acc. Chem. Res.*, 2020, **53**, 485–495.
29 Y. Cui, Y. Yue, G. Qian and B. Chen, *Chem. Rev.*, 2012, **112**, 1126–1162.
30 T. N. Nguyen, F. M. Ebrahim and K. C. Stylianou, *Coord. Chem. Rev.*, 2018, **377**, 259–306.
31 Z. Hu, B. J. Deibert and J. Li, *Chem. Soc. Rev.*, 2014, **43**, 5815–5840.
32 T. Rasheed and F. Nabeel, *Coord. Chem. Rev.*, 2019, **401**, 213065.
33 E. A. Dolgopolova, A. M. Rice, C. R. Martin and N. B. Shustova, *Chem. Soc. Rev.*, 2018, **47**, 4710–4728.
34 Z. Jia, Z. Han, K. Wang, T. Zhou, H. Min, T. Sun, Y. Liao, L. Wang, P. Cheng and W. Shi, *Inorg. Chem.*, 2022, **61**, 14313–14321.
35 C. W. Kung, S. Goswami, I. Hod, T. C. Wang, J. Duan, O. K. Farha and J. T. Hupp, *Acc. Chem. Res.*, 2020, **53**, 1187–1195.
36 D. Ren, H.-L. Xia, K. Zhou, S. Wu, X.-Y. Liu, X. Wang and J. Li, *Angew. Chem., Int. Ed.*, 2021, **60**, 25048–25054.
37 C. Fiankor, J. Nyakuchena, R. S. H. Khoo, X. Zhang, Y. Hu, S. Yang, J. Huang and J. Zhang, *J. Am. Chem. Soc.*, 2021, **143**, 20411–20418.
38 A. Juris, V. Balzani, F. Barigelletti, S. Campagna, P. Belser and A. von Zelewsky, *Coord. Chem. Rev.*, 1988, **84**, 85–277.
39 C. Wang, Z. Xie, K. E. deKrafft and W. Lin, *J. Am. Chem. Soc.*, 2011, **133**, 13445–13454.
40 T. C. Zhuo, Y. Song, G. L. Zhuang, L. P. Chang, S. Yao, W. Zhang, Y. Wang, P. Wang, W. Lin, T. B. Lu and Z. M. Zhang, *J. Am. Chem. Soc.*, 2021, **143**, 6114–6122.
41 G. Lan, Z. Li, S. S. Veroneau, Y. Y. Zhu, Z. Xu, C. Wang and W. Lin, *J. Am. Chem. Soc.*, 2018, **140**, 12369–12373.
42 D. Kim, D. R. Whang and S. Y. Park, *J. Am. Chem. Soc.*, 2016, **138**, 8698–8701.
43 Z. H. Yan, M. H. Du, J. Liu, S. Jin, C. Wang, G. L. Zhuang, X. J. Kong, L. S. Long and L. S. Zheng, *Nat. Commun.*, 2018, **9**, 3353.
44 M. Elcheikh Mahmoud, H. Audi, A. Assoud, T. H. Ghaddar and M. Hmadeh, *J. Am. Chem. Soc.*, 2019, **141**, 7115–7121.
45 T. Toyao, M. Saito, S. Dohshi, K. Mochizuki, M. Iwata, H. Higashimura, Y. Horiuchi and M. Matsuoka, *Chem. Commun.*, 2014, **50**, 6779–6781.
46 S. Zhang, L. Li, S. Zhao, Z. Sun and J. Luo, *Inorg. Chem.*, 2015, **54**, 8375–8379.
47 A. Kobayashi, Y. Suzuki, T. Ohba, T. Ogawa, T. Matsumoto, S. Noro, H. C. Chang and M. Kato, *Inorg. Chem.*, 2015, **54**, 2522–2535.
48 D. Luo, T. Zuo, J. Zheng, Z.-H. Long, X.-Z. Wang, Y.-L. Huang, X.-P. Zhou and D. Li, *Mater. Chem. Front.*, 2021, **5**, 2777–2782.
49 L. Martins, L. K. Macreadie, D. Sensharma, S. Vaesen, X. Zhang, J. J. Gough, M. O'Doherty, N. Y. Zhu, M. Ruther, J. E. O'Brien, A. L. Bradley and W. Schmitt, *Chem. Commun.*, 2019, **55**, 5013–5016.
50 D. Huo, F. Lin, S. Chen, Y. Ni, R. Wang, H. Chen, L. Duan, Y. Ji, A. Zhou and L. Tong, *Inorg. Chem.*, 2020, **59**, 2379–2386.
51 J. Hao, X. Xu, H. Fei, L. Li and B. Yan, *Adv. Mater.*, 2018, **30**, e1705634.
52 H. Zhang, J. Nai, L. Yu and X. W. Lou, *Joule*, 2017, **1**, 77–107.
53 X. Guo, X. Wan, Q. Liu, Y. Li, W. Li and J. Shui, *eScience*, 2022, **2**, 304–310.
54 P. Deria, J. E. Mondloch, O. Karagiaridi, W. Bury, J. T. Hupp and O. K. Farha, *Chem. Soc. Rev.*, 2014, **43**, 5896–5912.

55 S. M. Cohen, *J. Am. Chem. Soc.*, 2017, **139**, 2855–2863.
56 W. Li, W. Fang, C. Wu, K. N. Dinh, H. Ren, L. Zhao, C. Liu and Q. Yan, *J. Mater. Chem. A*, 2020, **8**, 3658–3666.
57 Q. Wang, J. Lu, Y. Jiang, S. Yang, Y. Yang and Z. Wang, *Chem. Eng. J.*, 2022, **443**, 136483.
58 S. Rezaee and S. Shahrokhian, *Appl. Catal., B*, 2019, **244**, 802–813.
59 S. V. Eliseeva and J. C. Bunzli, *Chem. Soc. Rev.*, 2010, **39**, 189–227.
60 L.-J. Xu, G.-T. Xu and Z.-N. Chen, *Coord. Chem. Rev.*, 2014, **273–274**, 47–62.
61 D. Guo, C. Y. Duan, F. Lu, Y. Hasegawa, Q. J. Meng and S. Yanagida, *Chem. Commun.*, 2004, 1486–1487, DOI: **10.1039/b403519d**.
62 M. D. Ward, *Coord. Chem. Rev.*, 2007, **251**, 1663–1677.
63 M. C. So, G. P. Wiederrecht, J. E. Mondloch, J. T. Hupp and O. K. Farha, *Chem. Commun.*, 2015, **51**, 3501–3510.